# Three-dimensional Heisenberg model with Dzyaloshinskii-Moriya interaction: A Monte Carlo study

G. Albuquerque Silva,[1] A. R. Bergeron,[2] J. A. Plascak,[1,2,3] and D. P. Landau[2]

[1]*Departamento de Física, Instituto de Ciências Exatas, Universidade Federal de Minas Gerais, C.P. 702, 30123-970 Belo Horizonte MG, Brazil*

[2]*Center for Simulational Physics, The University of Georgia, Athens, Georgia 30602 USA*

[3]*Universidade Federal da Paraíba, Centro de Ciências Exatas e da Natureza–Campus I, Departamento de Física–CCEN Cidade Universitária 58051-970, João Pessoa PB, Brazil*

(Received 28 December 2023; accepted 21 May 2024; published 6 June 2024)

The three-dimensional classical Heisenberg model on a simple cubic lattice with Dzyaloshinskii-Moriya (DM) interactions between nearest-neighbors in all directions has been studied using Monte Carlo simulations. The Metropolis algorithm, combined with single histogram reweighting techniques and finite-size scaling analyses, has been used to obtain the thermodynamic behavior of the system in the thermodynamic limit. Simulations were performed with the same set of interaction parameters for both *shifted* boundary conditions (SBC) and *fluctuating* boundary conditions (FBC). Because of an incommensurability caused by the DM interaction, the SBC incorporated a fixed shift angle at the boundary which varies as a function of the DM interaction and lattice size. This SBC method decreases the simulation time significantly, but the distribution of states is somewhat different than that obtained with FBC. The ground state for nonzero DM interaction is a spiral configuration where the spins are restricted to lie in planes perpendicular to the DM vector. We found that this spiral configuration undergoes a conventional second-order phase transition into a disordered, paramagnetic state with the transition temperature being a function of the magnitude of the DM interaction. The limiting case with only DM interaction in the model has also been considered. The critical exponent $\nu$, the critical exponent ratios $\alpha/\nu$, $\beta/\nu$, $\gamma/\nu$, as well as the critical temperature $T_c$ and fourth-order cumulant of the order parameter $U_4^*$ at $T_c$ have been estimated for different magnitudes of DM interaction. The critical exponents and cumulants at the transition are different from those for the three-dimensional Heisenberg model, but the ratios $\alpha/\nu$, $\beta/\nu$, $\gamma/\nu$, $U_4^*/\nu$ are the same, implying that weak universality is valid for all values of DM interaction. Structure factor calculations for particular cases have been performed considering SBC and FBC in the simulations with different lattice sizes at the critical temperatures.

DOI: 10.1103/PhysRevE.109.064113

## I. INTRODUCTION

The phenomenon giving rise to a spontaneous magnetization in the absence of an external magnetic field in ferromagnetic (FM) materials below the critical temperature was first elucidated by Heisenberg [1], who introduced a symmetric "exchange interaction" or, as he named it, "exchange term." In this way, not only ferromagnetic but antiferromagnetic (AFM) materials could be successfully analyzed based on models which incorporate an exchange interaction. A good example is the Heisenberg model itself. It was later noticed that a type of "weak" ferromagnetism occurs in certain antiferromagnetic materials that could not be explained only on the basis of the Heisenberg exchange interaction [2,3]. The agent responsible for this effect was clarified by Dzyaloshinskii [4] and Moriya [5] and is now called the Dzyaloshinskii-Moriya (DM) interaction.

It is interesting to note that, besides the antiferromagnetic materials exhibiting weak ferromagnetism, the DM interaction can also appear due to symmetry breaking at a surface of some magnetic materials [6], crystals with a chiral magnetic structure [7–10], and in magnetic thin films in multilayers [11–14]. In these cases, different magnetic phases than the usual FM phase can emerge, such as helical, conical, solitons, spiral phases, and even phases with more exotic spin textures like skyrmions [14,15]. Because of the importance of DM interactions to the formation of such novel and compelling spin textures, many experimental studies of systems with DM coupling have focused on these magnetic structural properties [16]. In addition, multiferroics (see, e.g., Ref. [17]), for which DM interaction plays a significant role, also exhibit other interesting behavior, e.g., ferroelectricity, which has captured the interest of experimentalists. The specific heat has been measured [18] for the ferromagnet $Mn_5Ge_3$, which orders at room temperature, but the resolution was insufficient to extract critical exponents of the respective second-order phase transition.

The thermodynamic properties, the magnetic structures, and the magnetic excitations present in these systems containing DM interaction have been studied by theoretical approaches as well as by Monte Carlo (MC) simulations (see, e.g., Refs. [19–24] and [25–30], respectively). However, in some of these investigations the important question of the weak universality class of the models has not been completely addressed when one regards the effect of the DM interaction.

In previous works [31,32], the two-dimensional XY model with DM interactions has been studied using MC simulations and finite-size scaling. The phase diagram in the temperature

 ©2024 American Physical Society

versus DM interaction plane, as well as the respective critical exponents were obtained, and it was noticed that the modulation of the spin vectors with position depended upon the value of the DM interaction. As a result, incommensurability may appear when arbitrary values of the DM interaction are considered in the simulations. In this case, fluctuating boundary conditions (FBC) have been implemented in order to properly accommodate incommensurabilities.

Here we have adopted the same procedure used for the two-dimensional XY model to analyze the Heisenberg model with DM interaction in three dimensions. As stated by Moriya [5], DM interactions occur in crystals of low symmetry, like noncentrosymmetric crystals [6]. Despite some special details that occur in real materials, e.g., intrinsic interaction anisotropies and crystal asymmetries, we have considered a simpler model consisting of the traditional isotropic exchange Heisenberg Hamiltonian with DM interaction defined in a simple cubic lattice. This model has some similarity with the pyrochlore lattice with DM interactions [33] (in spite of the difference of lattice symmetry, which is hexagonal in the later one [34]). Besides that, several chiral helimagnets, among which MnSi and $CrNb_3S_6$, have been studied on the basis of simpler models like the one considered here [25–30], having subtle differences with respect to the way that DM vector interactions are defined between the spins in the lattice and/or by the addition of extra interaction terms in the model.

The plan of the paper is as follows: In the next section, the model and effective Hamiltonian are presented. Section III is devoted to the methodology, including the Monte Carlo simulation details, boundary conditions, thermodynamic quantities of interest, and finite-size scaling analyses. The results are presented in Sec. IV and concluding remarks are made in the final section.

## II. MODEL

The Hamiltonian we have considered can be written as

$$\mathcal{H} = -J \sum_{\langle i,j \rangle} \mathbf{S}_i \cdot \mathbf{S}_j - \sum_{\langle i,j \rangle} \mathbf{D} \cdot (\mathbf{S}_i \times \mathbf{S}_j), \tag{1}$$

where the first sum represents the isotropic Heisenberg term with exchange interaction $J$, and the second sum represents the Dzyaloshinskii-Moriya term, with $\mathbf{D}$ being the DM vector interaction. $\mathbf{S}_i$ are three-dimensional classical spin vectors sitting at each site $i$ of a simple cubic lattice with $\|\mathbf{S}_i\| = 1$. The bracket $\langle i, j \rangle$ specifies that each spin interacts with its nearest neighbors along the three directions of the lattice for both for the FM and DM interactions.

Choosing the DM vector along the positive $z$ direction and applying the transformation proposed by Alcaraz and Wreszinski [35], we get the effective Hamiltonian

$$\mathcal{H}(d) = -J \sum_{\langle i,j \rangle} \{\sqrt{1+d^2}\cos[\varphi_i - \varphi_j - \phi(d)] \times \sin\theta_i \sin\theta_j + \cos\theta_i \cos\theta_j\}, \tag{2}$$

where $d = D/J$, $D$ is the magnitude of the DM interaction vector, $\varphi_i$ and $\theta_i$ are the angles of the spin vector $\mathbf{S}_i$ in spherical coordinates, and $\phi(d) = \tan^{-1} d$. It is worthwhile to stress, for future reference, that the Hamiltonian (2) is equivalent to an anisotropic Heisenberg model with renormalized exchange interaction in the $x$-$y$ plane.

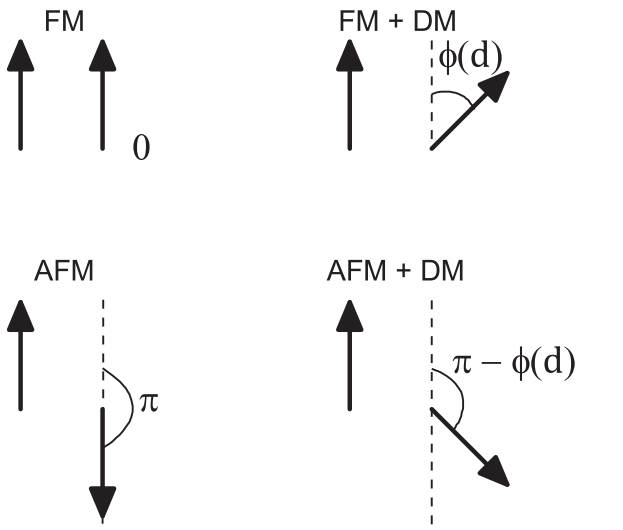


FIG. 1. A simple illustration showing the ground-state relative orientation of two nearest spin vectors according to the type of interaction between them. Top illustrations for the ferromagnetic case (FM) case, with and without Dzyaloshinskii-Moriya (DM) interactions. Bottom illustrations for the antiferromagnetic (AFM) case, with and without DM interaction. The azimuthal angular difference $\phi(d)$ of the pair of spins is indicated in each case.

It is easy to see that, in the FM ($J > 0$) ground state all the spin vectors arrange themselves in a spiral configuration where the spins are restricted to lie in planes perpendicular to the DM vector. Moreover, two adjacent spin vectors have an angular difference equal to $\phi(d)$. As depicted in the top sketches in Fig. 1, and one lattice spacing displacement implies that a $\phi(d)$ rotation of the next spin vector, causes a modulation of the $x$- and $y$- spin components along the principal lattice directions, which causes a modulation on the $x$- and $y$-spin components along the $x$-, $y$-, and $z$-lattice directions. In this sense, $\phi(d)$ is the pitch angle and, according to its value, the modulation length may be either commensurate or incommensurate with a finite lattice. It is this possible incommensurability that requires more subtle boundary conditions when simulating the model with DM interaction on finite lattices.

In the AFM case, i.e., $J < 0$, the ground-state configuration of the model would also be restricted to lie in planes perpendicular to the DM vector, but the spin vectors now would arrange themselves in an antiparallel way, with any spin and its nearest neighbor in the lattice having an azimuthal angular difference equal to $\pi - \phi(d)$, as it is depicted in the bottom sketches in Fig. 1. This means that one lattice spacing displacement implies in a $\pi - \phi(d)$ rotation of the next spin vector, giving rise to a modulation on the spin vectors as discussed in the above paragraph. Some attention should be paid to the signal of $\phi(d)$ in Eq. (2), which changes into $-\phi(d)$ in the cosine argument due to the ratio $d = D/J$.

This work will be focused only on the FM case, though the AFM case could be studied in a very similar approach and eventually lead to similar conclusions about the critical behavior of the antiferromagnetic model with DM interaction.

## III. METHODOLOGY

### A. Monte Carlo simulations

The simulations consist of running several MC steps per spin (MCS) and storing the corresponding values of energy, order parameter, etc. One MCS is defined by a sequential sweep of all the spins of the lattice using the standard Metropolis algorithm [36]. For each spin vector $\mathbf{S}_i$ having angles $(\theta_i, \varphi_i)$, new angles $(\theta_i', \varphi_i')$ are randomly chosen and accepted if the total energy becomes smaller than the total energy for the previous angles or if the Boltzmann probability of the energy difference is greater than a random number uniformly distributed between 0 and 1. If this last condition does not occur, then the spin angles remain unchanged.

Lattices with $L \times L \times L = L^3$ sites have been used in the MC simulations with the sizes raging from $L = 8$ to 56 ($L = 64$ in some cases). A typical simulation consisted of $10^5$–$10^6$ discarded MCS (depending on $L$) for thermalization and measurements taken every 10 MCS within the total of $10^6$ MCS after equilibration. For some finer analysis, single-histogram reweighting techniques were used with data from 300 to 800 simulations (again, depending on $L$), running on different processor cores and starting with different random number generator seeds. A maximum of $1.6 \times 10^9$ configurations have been generated for the lattice size $L = 56$, with histograms constructed with data coming from $8 \times 10^7$ configurations. The random number generator we have used was "ran2" in Ref. [37].

### B. Boundary conditions

To check if the modulation length due to the DM interaction, measured by the parameter $d$, is commensurate or incommensurate with the lattice size $L$, we considered a shift angle $\Delta(d, L)$ in the interval $[0, 2\pi)$, given by

$$\Delta(d, L) = \mathrm{mod}[L\phi(d), 2\pi], \tag{3}$$

where $\phi(d)$ is the pitch angle and "mod" is the modulo operation. In the case of the ground-state spin configuration at $T = 0$, if $\Delta(d, L) = 0$, then the configurations are commensurate with the lattice. Otherwise, when $\Delta(d, L)$ differs from zero, an incommensurability takes place. However, having this shift angle at hand, it is possible to compensate the azimuthal angular differences $\varphi_i - \varphi_j$, for the spins $i$ and $j$ along the boundary of the lattice, by choosing $\varphi_i + \Delta - \varphi_j$. If one wishes to study the AFM version of the model, then it would only be necessary to make the change $\phi(d) \to \pi - \phi(d)$ in Eq. (3).

Based on these considerations, we have defined two different boundary conditions for the simulations. One uses $\Delta$ calculated from Eq. (3), which remains fixed during the entire simulation. The other one uses a variable value of $\Delta$ which is calculated by an extra Metropolis step specially designed for the spins on the boundary of the lattice. For convenience, we will refer to the use of a constant $\Delta$ as *shifted boundary condition* (SBC) and FBC [38] when $\Delta$ is determined through an extra Metropolis sweep. For the simulations with FBC, we defined $\Delta_x$, $\Delta_y$, and $\Delta_z$ to be the shift angles for each direction in the lattice and they were calculated independently of each other. In this way, after one MCS with Metropolis algorithm, there is one additional step to sweep all the spins along the boundary to compute the three shift angles.

We stress here that, whenever $\Delta(d, L) = 0$, SBC becomes identical to the usual periodic boundary condition (PBC). For instance, the configurations are commensurate with the lattice sizes for (i) $d = 0$ for any value of $L$ because $\phi = 0$, (ii) $d = 1$ for $L$ being a multiple of 8 since $\phi = \pi/4$, and (iii) $d = \infty$ for $L$ multiple of 4 since $\phi = \pi/2$. In all cases above SPC and PBC produce the same result. However, for $d = 0.5$, for example, a spin modulation length equal to $2\pi / \tan^{-1} 0.5 = 13.55\ldots$ lattice spacing results in an unavoidable incommensurability case for any finite lattice size.

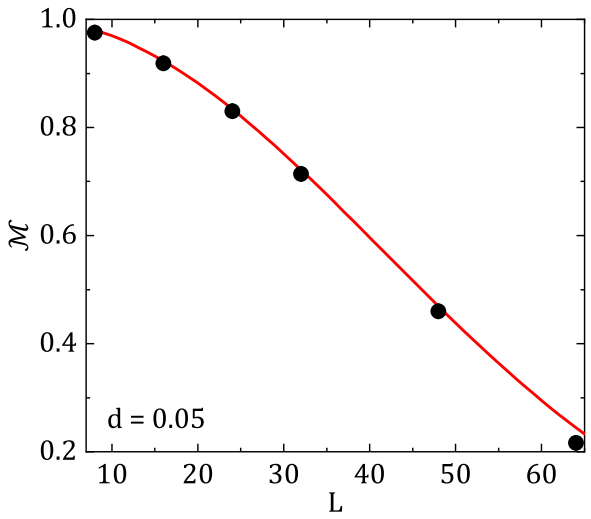


FIG. 2. Magnetization per spin $\mathcal{M}$ as a function of the lattice size $L$ for a small value $d = 0.05$. The solid line corresponds to the theoretical result at $T = 0$, given by Eq. (4) in a simple cubic lattice. The circles are MC simulation results at a low temperature $T = 0.025$. The MC errors are smaller than the symbol sizes.

### C. Thermodynamic quantities and finite-size scaling relations

In this model, the usual magnetization per spin $\mathcal{M}$, defined as the magnitude of the vectorial sum of all spins $\mathbf{S}_i$ divided by the number of sites, $\mathcal{M} = \| \sum_{i=1}^{L^3} \mathbf{S}_i \| / L^3$, goes to zero in the thermodynamic limit as soon as $d \neq 0$. Nevertheless, for finite lattices this quantity differs from zero. At $T = 0$, where all spins are in the $x$-$y$ plane, it is possible to compute $\mathcal{M}$ as a function of $L$ and $\phi$. The result is

$$\mathcal{M}(L, \phi) = \left| \frac{\sin(L\phi/2)}{L \sin(\phi/2)} \right|^3. \tag{4}$$

It is clear that $\mathcal{M}(L, \phi) \to 0$ as $L \to \infty$ for any finite $\phi$. As $\phi \to 0$ one has $\mathcal{M}(L, \phi) \to 1$, as expected, because, in this case, we have $d = 0$ and the DM interaction is suppressed.

The full line in Fig. 2 gives the behavior of $\mathcal{M}$ from Eq. (4), as a function of the lattice size $L$, for a small pitch angle corresponding to $d = 0.05$. The circles correspond to MC results for the same value of $d$ and for a very low temperature $T = 0.025$. Here, and in the remainder of this paper, we consider the exchange interaction $J = 1$ and the Boltzmann constant $k_B = 1$ (in other words, it simply means that we are measuring

the temperature $T$ in convenient units of $k_B/J$). The agreement seen in this figure shows that $T = 0.025$ is low enough to capture the essence of the ground-state configuration.

Even when the temperature increases from such a low value, the spin vectors are still forced to closely stay in planes perpendicular to the DM vector. This can be seen from the behavior of the $z$-component magnetization $\mathcal{M}_z = (\sum_{i=1}^{L^3} S_i^z)/L^3$ as the temperature increases. Figure 3 shows the results from MC simulations at $d = 0.05$ and $d = 0.5$ and different lattice sizes. $\mathcal{M}_z$ fluctuates around zero with the magnitude of its fluctuation decreasing as $d$ increases in the whole temperature range. Furthermore, $\mathcal{M}_z$ seems to tend to zero as the lattice size tends to infinity. It is also interesting to notice that the DM interaction forces the spins to stay in perpendicular planes even for smaller lattices, since the fluctuations decrease two orders of magnitude when $d = 0.5$ even for the smaller lattice $L = 8$.

Based on the foregoing considerations, it is evident that the magnetization per spin $\mathcal{M}$ cannot be used as an order parameter as soon as one has a DM interaction in the model (despite the fact that, as the temperature increases, the magnetization per spin decreases from its value at $T = 0$ for each value $L$ and approaches zero).

We have defined a different order parameter $m$ as

$$m = \frac{1}{L^3}\sqrt{\left\{\sum_{i=1}^{L^3}\cos[\varphi_i + (x_i + y_i + z_i)\phi]\sin\theta_i\right\}^2 + \left\{\sum_{i=1}^{L^3}\sin[\varphi_i + (x_i + y_i + z_i)\phi]\sin\theta_i\right\}^2 + \left(\sum_{i=1}^{L^3}\cos\theta_i\right)^2}. \quad (5)$$

Note that $m$ depends not only on the spin spherical angles but also on their positions in the lattice and the pitch angle $\phi$. Ultimately, the terms $(x_i + y_i + z_i)\phi$ in Eq. (5) have the effect of undoing the modulations on the spin vectors caused by the presence of the DM interaction, with $x_i, y_i, z_i \in [0, L-1]$. As a result, for any finite lattice $m = 1$ in the ground state and decreases to zero as the temperature increases, playing the perfect role of an order parameter.

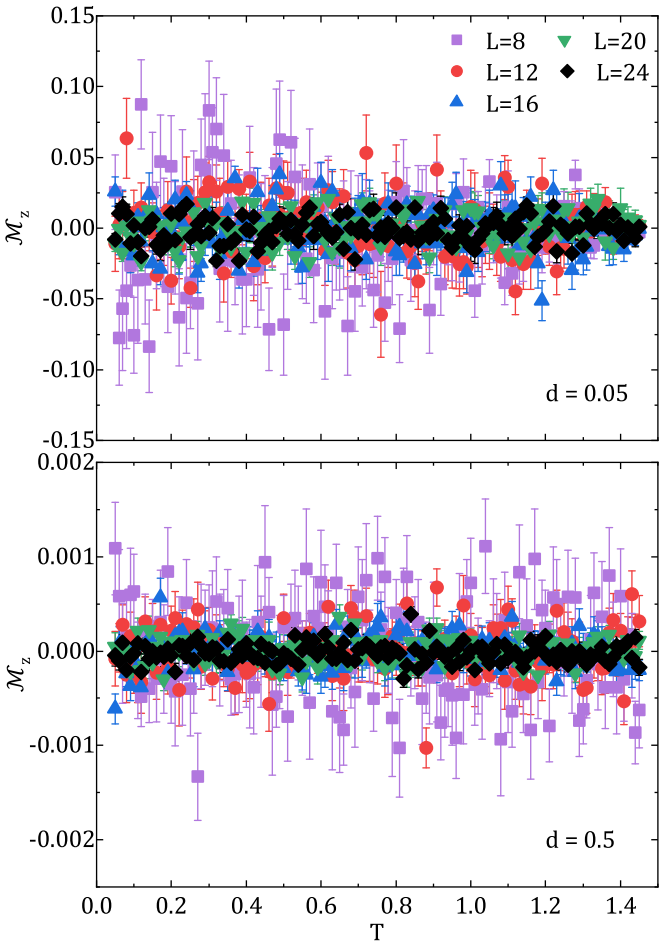


FIG. 3. MC results of the $z$-component magnetization per spin $\mathcal{M}_z$, as a function of the temperature $T$, for different lattice sizes, at $d = 0.05$ (top panel) and $d = 0.5$ (bottom panel).

A very useful quantity to compute the critical temperature is the fourth-order (Binder) cumulant of the above order parameter [39], defined in its reduced form as

$$U_4 = 1 - \frac{\langle m^4\rangle}{3\langle m^2\rangle^2}, \quad (6)$$

where the angle brackets denote the thermal average. For sufficiently large systems, this cumulant as a function of temperature should cross at the same point $T_c$ for different values of $L$. $T_c$ is thus the critical temperature and the cumulant $U_4^*$ at $T_c$ has a universal value. In addition, the slopes of $U_4$ at $T_c$ are proportional to $L^{-1/\nu}$, where $\nu$ is the correlation length critical exponent. These properties of $U_4$ allow an almost unbiased estimate of $T_c$, $U_4^*$ and $\nu$ [40,41].

When the finite lattices are not large enough, residual corrections to finite-size scaling (FSS) [39] make the crossing points of the cumulant $U_4$ suffer a systematic shift as $L$ varies. As we shall see below, this also happens in the present model. However, if $T_{\rm cross}(L, L_s)$ is the crossing temperature of the cumulants for lattice sizes $L$ and $L_s$, where $L_s$ is fixed and taken as a reference lattice size, then the systematic deviations of this quantity can be modeled as [40,41]

$$T_{\rm cross}(L, L_s) = T_c(\infty, L_s) + \frac{B_T}{\log_{10}(L/L_s)}, \quad (7)$$

where $T_c(\infty, L_s)$ gives us an estimate of the critical temperature of the infinite system and $B_T$ is a nonuniversal constant.

Similarly to Eq. (7), the cumulant values at $T_{\rm cross}(L, L_s)$, namely $U_4^*(L, L_s)$, can be modeled as

$$U_4^*(L, L_s) = U_4^*(\infty, L_s) + \frac{B_U}{\log_{10}(L/L_s)}, \quad (8)$$

where $U_4^*(\infty, L_s)$ provides an estimate of the cumulant for the infinite lattice and $B_U$ is another nonuniversal constant.

Since both $T_c(\infty, L_s)$ and $U_4^*(\infty, L_s)$ could still depend on the reference lattice $L_s$, one eventually obtains the critical

temperature $T_c$ and the fourth-order cumulant $U_4^*$ in the limit $L_s \to \infty$, namely $T_c = T_c(\infty, \infty)$ and $U_4^* = U_4^*(\infty, \infty)$. In the present case, it was possible to get reasonable resolution for the cumulant crossings with $L_s = 8,\ 12,\ 16$, and 20. We have also taken $L > L_s$ for all values of $L_s$.

Having the critical temperature in hand, the critical exponents of the correlation length $\nu$, order parameter $\beta$, susceptibility of the order parameter $\gamma$, and specific heat $\alpha$ can be computed from the finite-size scaling relations,

$$\left.\frac{dU_4(\beta_T;L)}{d\beta_T}\right|_{\beta_T=\beta_{T_c}} \approx\ U_0 L^{-1/\nu}, \tag{9}$$

$$m(T = T_c; L) \approx\ m_0 L^{-\beta/\nu}, \tag{10}$$

$$\chi_{\text{peak}}(L) \approx\ \chi_0 L^{\gamma/\nu}, \tag{11}$$

$$C_{\text{peak}}(L) \approx\ C_\infty + C_0 L^{\alpha/\nu}, \tag{12}$$

where $U_0$, $m_0$, $\chi_0$, $C_\infty$, and $C_0$ are constants. Equation (9) corresponds to the derivative of the fourth-order cumulant with respect to the variable $\beta_T = 1/k_B T$ and is taken at the critical temperature. Equation (10) is the order parameter at $T_c$. Equation (11) is the peak value of the order parameter susceptibility $\chi$ defined by

$$\chi = \frac{L^3[\langle m^2\rangle - \langle m\rangle^2]}{k_B T}, \tag{13}$$

and Eq. (12) is the peak value of the specific heat $C$ given by

$$C = \frac{\langle \mathcal{H}^2\rangle - \langle \mathcal{H}\rangle^2}{L^3 k_B T^2}. \tag{14}$$

More detail about the nature of the phase transition is given by the structure factor [41], which provides information about the spin-spin correlations and the magnetic long-range ordering. This quantity is defined by the spatial Fourier transform of the time-independent pair-correlation function $\Gamma(\mathbf{r}_{jk}) = \langle \mathbf{S}_j \cdot \mathbf{S}_k\rangle - \langle \mathbf{S}_j\rangle \cdot \langle \mathbf{S}_k\rangle$ of the spin configurations in thermal equilibrium, with $\mathbf{r}_{jk} = \mathbf{r}_j - \mathbf{r}_k$ being the relative vector position of the spins at $j$ and $k$ sites, respectively (the lattice parameter has been normalized to unity). Accordingly, the static structure factor $\mathcal{S}(\mathbf{q})$ can be written as

$$\mathcal{S}(\mathbf{q}) = \frac{1}{L^3}\sum_{j,k} \Gamma(\mathbf{r}_{jk}) e^{i\mathbf{q}\cdot\mathbf{r}_{jk}}, \tag{15}$$

where $\mathbf{q}$ is the wave vector and the double summation runs over all the spins in the lattice. This structure factor is also very useful to investigate the magnetic structures emerging from complex arrangements of the spins, as well as distinguishing different magnetic phases [42,43].

### D. More on simulations

The simulations have been done following two different approaches for different values of $d$ and shifted and fluctuating boundary conditions.

In the first approach, data generated by sets of extensive MC simulations as described above (with an estimated CPU time of the order $7 \times 10^5$ core-hours), together with the single histogram reweighting, have been used to accurately estimate the critical temperature $T_c$ and the value of the fourth-order cumulant $U_4^*$. For this purpose, we have used Eqs. (5)–(8) with $L \leqslant 56$. The critical exponent $\nu$ and the ratio $\beta/\nu$ have been estimated through the FSS relations given by Eqs. (9) and (10).

In the second approach, with less computational effort (an estimated $10^5$ core-hours), the susceptibility of the order parameter and specific heat curves as a function of $T$ have been directly obtained from single MC simulations, and the ratios $\gamma/\nu$ and $\alpha/\nu$ have been estimated from the FSS relations given by Eqs. (11) and (12). In this case we have also included a larger lattice $L = 64$. Additional estimates of $T_c$, using the FSS of the temperatures where the susceptibility of the order parameter and specific heat take place, have been obtained as well. The computation of the structure factor $\mathcal{S}(\mathbf{q})$ has been done following this second approach for lattice sizes $L \leqslant 24$ (CPU time of only about 2000 core-hours in this case).

## IV. RESULTS

In this section, we will focus on the results for three particular regimes of $d$. The first one is when $d = 0$ which is the well-known Heisenberg model that has no spin modulation but only FM order at low temperatures. In this case, comparison of the present results with previous simulations can also be made. As an intermediate regime, we consider $d = 0.5$, having a spin modulation length that results in an unavoidable incommensurability for any finite lattice size. In some cases, $d = 1$ will also be considered, where commensurate lattices are obtained when $L$ is a multiple of 8.

The third regime is when $d$ tends to infinity and the DM interaction dominates, i.e., a three-dimensional "DM model" containing only DM interactions. This regime will be referred to as $d = \infty$, where the second term involving cosines in Eq. (2) can be neglected. This case results in the shortest possible spin modulation length $\phi = \pi/2$ being equal to four lattice spacings. The incommensurability can thus be circumvented by choosing lattice sizes $L = 4n$, with $n = 1, 2, \ldots$.

In the $d = \infty$ limit, where the cosines term can be neglected, the simulations provide a transition where

$$[\beta_{T_c} J\sqrt{1 + d^2}]^{-1} = T_c^{\text{DM}} \tag{16}$$

plays the role of the critical temperature of the DM model. In addition, from Eq. (16) one has (recalling that we are considering $k_B = 1$ and $J = 1$)

$$T_c = T_c^{\text{DM}} d. \tag{17}$$

The above equation also gives the slope of the transition temperature line $T_c(d)$, as a function of $d$, in the $d = \infty$ limit. This feature will become clearer below, when discussing the global phase diagram.

In all the above three different regimes, we consider both SBC and FBC and compare their respective results.

### A. Energy and order parameter distribution functions

In all the below data, the histograms have been analyzed within the desired temperature interval, e.g., around the cumulant crossings. We, thus, checked if the energy and order parameter distributions maintain their shapes and are free from any noise at their tails as compared to the original

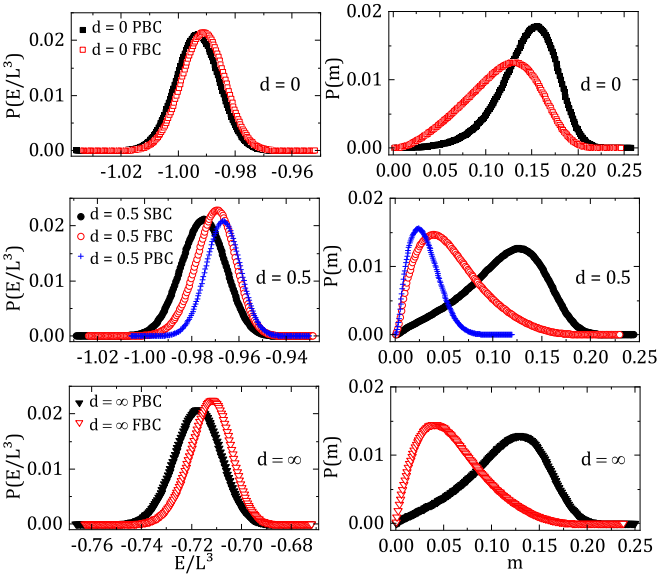


FIG. 4. Probability distributions of the energy per site $P(E/L^3)$ (left panels) and order parameter $P(m)$ (right panels) for values of $d$ in the three chosen regimes and both SBC and FBC. The lattice size is $L = 48$ and the temperature is close to the critical temperature for each DM interaction. The middle panels for $d = 0.5$ also show the probability distribution with periodic boundary conditions (PBC). The legends on the left panels also apply to the right panels.

distributions at the temperature where the Monte Carlo simulations have been performed. As the crossing temperatures were not so far away from each other and from the temperature where the histograms were taken, and due to the sufficient amount of data from the MC simulations, no problems were observed in the distributions for any lattice sizes.

As an example, Fig. 4 show the energy per site and order parameter probability distribution function for the lattice size $L = 48$ in the three regimes of the DM interaction using both SBC and FBC. For each value of $d$, the probability distributions have been obtained using histograms at a temperature that is close to the critical temperature and different from the temperature where the histograms were measured. The smooth behavior of the curves shows that the temperature range is still within the region of validity. It is also clear that the shape of the distributions are indeed dependent on the type of the chosen boundary conditions.

Both $d = 0$ and $d = \infty$ are commensurate with the lattice size $L = 48$, and the use of either SBC or usual periodic boundary conditions (PBC) give the same result. The situation is different for $d = 0.5$, because there is an incommensurabilty with the lattice. The middle panels of Fig. 4 also show the corresponding probability distributions using PBC. However, the results with PBC for incommensurate lattices, shown in Ref. [32], do not produce coherent values with the expected FSS behavior. This can be clearly seen for $d = 0.5$, where $P(E/L^3)$ for PBC is clearly narrower with its $\chi^2$ smaller than the other boundary conditions, and $P(m)$ has much smaller width and wings, resulting in much different susceptibilities and fourth-order cumulants.

### B. Critical temperature $T_c$ and fourth-order cumulant $U_4^*$

Figure 5 shows the order parameter fourth-order cumulants, defined in Eq. (6), as a function of the temperature $T$ for $d = 0$, $d = 0.5$, and $d = \infty$. The temperature $T^{\rm DM}$, in the $d = \infty$ limit, is given by $T^{\rm DM} = [\beta_T J\sqrt{1+d^2}]^{-1}$. For each graph, there are two sets of curves constructed by using the histogram method and taking the data from MC simulations with SBC and FBC.

It is clear from Fig. 5 that, independent of the chosen boundary conditions, there are systematic deviations of the cumulant crossings for all considered values of $d$ as the lattice size changes. Nevertheless, it was possible to compute the crossing temperatures $T_{\rm cross}(L, L_s)$ for $L_s = 8$, 12, 16, and 20, with $L > L_s$. The values of $T_{\rm cross}(L, L_s)$ and their error bars have been estimated by approximating the cumulants as linear functions of $T$ in the regions where the crossings occur, with temperature steps $\Delta T = 0.0001$ (this procedure has already been used in a previous work [32] for the two-dimensional XY model). The above process has also been used in obtaining $T^{\rm DM}_{\rm cross}(L, L_s)$.

The results for the crossing temperatures $T_{\rm cross}(L, L_s)$ and $T^{\rm DM}_{\rm cross}(L, L_s)$, as a function of $[\log_{10}(L/L_s)]^{-1}$, are depicted in Fig. 6 for the three values of $d$ and using SBC and FBC. The straight lines are fits to Eq. (7) that provide a partial estimate of the critical temperature $T_c(\infty, L_s)$. We have different scaling behaviors for different reference lattices $L_s$. Although for $d = 0$ the FSS functions are comparable for SBC and FBC, for $d \neq 0$ different boundary conditions lead to different scaling behavior.

Despite the difference in the scaling functions shown in Fig. 6, in all cases the extrapolated temperatures smoothly converge to a single value as the reference lattice gets larger. This convergence can be seen in Fig. 7, which depicts the $T_c(\infty, L_s)$ and $T_c^{\rm DM}(\infty, L_s)$ as a function of $1/L_s$ obtained for the values of $d$ of Fig. 6, together with the results obtained for $d = 1$ with only SBC. One can clearly see that as $L_s$ gets larger, the critical temperature tends to a constant, furnishing then $T_c = T_c(\infty, \infty)$, for any value of $d$. In the process of obtaining $T_c$, the smaller reference lattice $L_s = 8$ has been neglected in all cases, and an average has been made only considering the remain lattice results having values that agree within the error bars. With this process, some results come only from the largest reference lattice $L_s = 20$. The numerical results of the final critical temperature, for each value of the DM interaction of Fig. 7, are also depicted in Table I. As expected, the estimated values of $T_c$ are the same, regardless of the type of boundary condition.

Evaluating the cumulants $U_4^*(L, L_s)$, and the corresponding errors at the crossing temperatures $T_{\rm cross}(L, L_s)$ or $T^{\rm DM}_{\rm cross}(L, L_s)$ is now straightforward using the already-computed histograms. In order to have the smallest possible errors, we have chosen the reference lattice $L_s$ to compute the fourth-order cumulants. Figure 8 shows $U_4^*(L, L_s)$, as a function of $[\log_{10}(L/L_s)]^{-1}$, at the crossing temperatures $T_{\rm cross}(L, L_s)$. The lines are linear fits using Eq. (8), from which one gets the extrapolated cumulant $U_4^*(\infty, L_s)$. As for the crossing temperatures, different FSS behaviors occur for each reference lattice $L_s$ and for all values of $d$. However, in this case, the extrapolated values of cumulants not only seem to depend

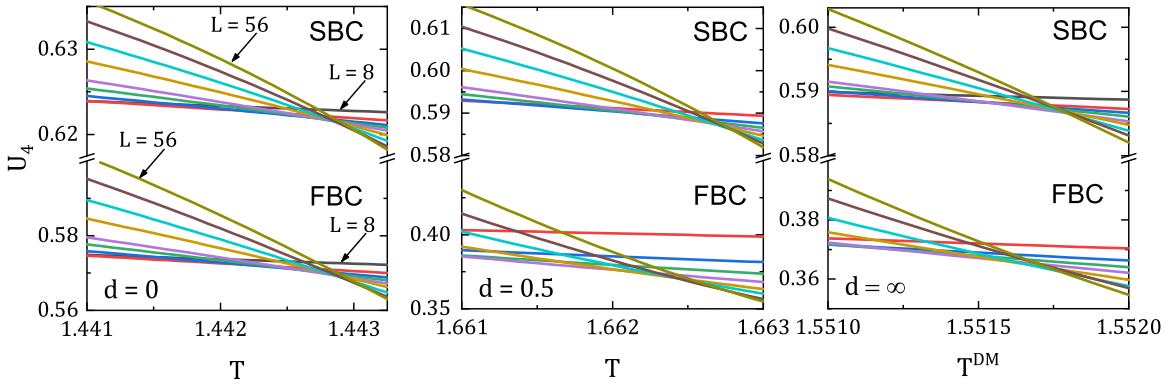


FIG. 5. Fourth-order cumulant of the order parameter $U_4$ as a function of temperature $T$ for $d = 0$ (left panel), $d = 0.5$ (middle panel), and $d = \infty$ (right: where $T^{\rm DM} = [\beta_T J\sqrt{1+d^2}]^{-1}$ in the $d = \infty$ limit). The lattice sizes range from $L = 8$ to $L = 56$, as specified in the text. In each panel, the top curves are for SBC and the bottom curves are for FBC (note the different axis scale for each boundary conditions). The lattice size pattern in the left panel also applies to the other two panels.

on the boundary conditions but also whether $d$ is zero or nonzero.

In order to better see the effects of the boundary conditions and the DM interaction on the cumulant value at the transition, Fig. 9 shows $U_4^*(\infty, L_s)$, as a function of $1/L_s$, for different values of $d$ and also $d = 1$ with SBC. It has been performed extra linear fits to estimate $U_4^*$, as it can be seen by the full straight lines in Fig. 9. In this procedure, the points with $L_s = 8$ have not been taken in the fits for all of the $d$ values and boundary condition, except for $d = 0.5$ FBC, which $U_4^*$ was obtained from the vertical axis intercept of the straight line defined by the points with $L_s = 16$ and $L_s = 20$. For this case, the error associated with the $U_4^*$ estimate was obtained by propagating the error from the two points used to define the straight line. For $d = 0$, the results are almost independent of $L_s$ for both boundary conditions, and the fits yield $U_4^* = 0.6208(1)$ for SBC and $U_4^* = 0.5679(2)$ for FBC. This is clear evidence that, as in other models, the cumulant does depend on the boundary conditions [32,44].

For $d > 0$, the finite-size effects become stronger, mainly for FBC. Interestingly, with SBC, for different values of $d$ the cumulants $U_4^*(\infty, L_s)$ clearly converge to the same result as $L_s$ gets larger. On the other hand, despite stronger finite-size behavior for FBC, the results also seem to converge to the same result but with a different value as compared to the SBC. The corresponding final estimates of the cumulants at the transition temperature for $d > 0$ with SBC and FBC are listed in Table I. It is clear from Table I that, for any $d > 0$, the cumulants at $T_c$ have the same value (within the error bars) with SBC. With FBC they are outside of the error bars

TABLE I. Final estimates of the critical temperature $T_c$, the value of the cumulant $U_4^*$ at $T_c$, the critical exponent $\nu$ and the ratios $\beta/\nu$, $\gamma/\nu$, and $\alpha/\nu$, for several values of $d$ and both SBC and FBC. $T_c^{C_{\rm peak}}$ and $T_c^{\chi_{\rm peak}}$ are also critical temperature estimates obtained from finite-size scaling analyses. Universal values are averages obtained from the top seven row data and also include the ratio $U_4^*/\nu_{\rm SBC}$ for SBC. Some results from the literature for the Heisenberg and XY models are also displayed for comparison.

| $d$ | $T_c$ | $U_4^*$ | $\nu$ | $\beta/\nu$ | $\gamma/\nu$ | $\alpha/\nu$ | $T_c^{C_{\rm peak}}$ | $T_c^{\chi_{\rm peak}}$ |
|---|---|---|---|---|---|---|---|---|
| 0 (SBC) | 1.44293(5) | 0.6208(1) | 0.713(2) | 0.5152(1) | 1.963(6) | −0.33(7) | 1.4419(6) | 1.4424(4) |
| 0 (FBC) | 1.44296(2) | 0.5679(2) | 0.710(1) | 0.5158(4) | 1.969(5) | −0.25(9) | 1.4420(4) | 1.4428(4) |
| 0.5 (SBC) | 1.66281(1) | 0.58434(9) | 0.670(2) | 0.5172(3) | 1.997(8) | −0.18(5) | 1.6621(4) | 1.6629(3) |
| 0.5 (FBC) | 1.66272(3) | 0.3488(2) | 0.6726(7) | 0.510(4) | 1.984(22) | −0.23(9) | 1.6629(2) | 1.6630(2) |
| 1 (SBC) | 2.14692(5) | 0.5854(1) | 0.677(2) | 0.5175(1) | | | | |
| ∞ (SBC) | 1.55183(1) | 0.5856(4) | 0.674(2) | 0.5186(4) | 1.968(15) | −0.24(9) | 1.5512(5) | 1.5517(4) |
| ∞ (FBC) | 1.55181(2) | 0.35836(4) | 0.673(3) | 0.515(1) | 1.951(12) | −0.29(11) | 1.5513(3) | 1.5521(3) |
| | | | | Our universal values | | | | |
| $d$ | $U_4^*$ (SBC) | $U_4^*$ (FBC) | $\nu$ | $\beta/\nu$ | $\gamma/\nu$ | $\alpha/\nu$ | $U_4^*/\nu_{\rm SBC}$ | Ref. |
| 0 | 0.6208(1) | 0.5679(2) | 0.712(2) | 0.5155(4) | 1.966(4) | −0.29(6) | 0.869(4) | |
| ≠ 0 | 0.5851(7) | 0.3536(69) | 0.673(3) | 0.516(3) | 1.975(20) | −0.24(5) | 0.872(2) | |
| | | | | Heisenberg model | | | | |
| 0 | 0.6202(1) | | 0.7112(5) | 0.5187(6) | 1.963(2) | −0.188(2) | 0.8727(6) | [47] |
| | 0.6217(8)[a] | | 0.712(4) | 0.515(5) | 1.972(7) | −0.192(16) | 0.873(5) | [48] |
| | | | | XY model | | | | |
| | 0.5859(8) | | 0.669(6) | 0.5179(24) | 1.965(5) | | 0.876(8) | [49] |
| | 0.5856(1) | | 0.6717(1) | 0.5190(2) | 1.9619(4) | −0.0225(5) | 0.8718(2) | [50] |

[a]From Ref. [40].

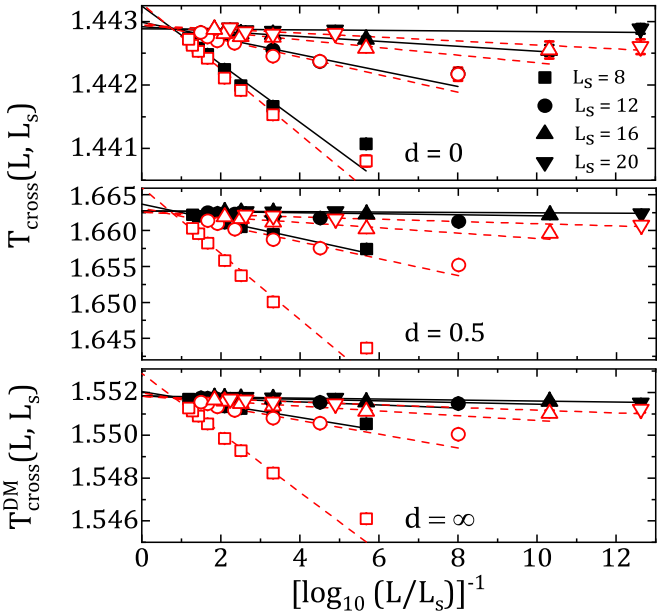


FIG. 6. Crossing temperatures $T_{\rm cross}(L, L_s)$ and $T^{\rm DM}_{\rm cross}(L, L_s)$, as a function of $[\log_{10}(L/L_s)]^{-1}$, for $d = 0$ (top panel), $d = 0.5$ (middle panel), and $d = \infty$ (bottom panel). Different symbols correspond to different reference sizes $L_s$. Full symbols and full lines correspond to SBC, while open symbols and dashed lines to FBC. Both types of lines are linear fits according to Eq. (7). The legend in the top panel also applies to the other panels. Where not shown, the error bars are smaller than the symbol sizes.

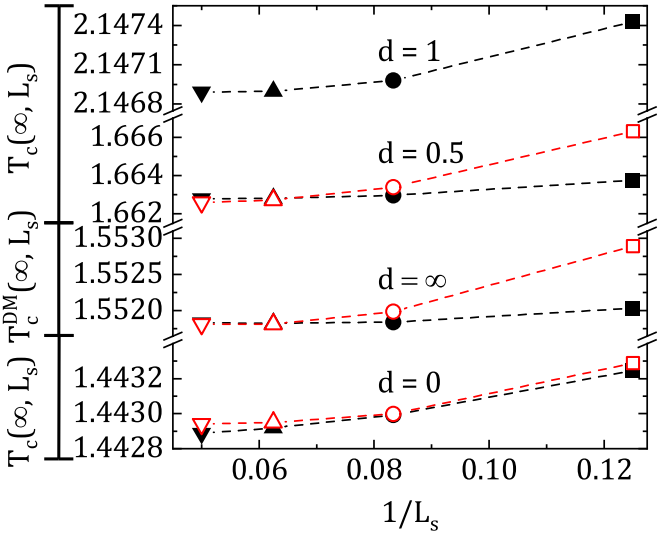


FIG. 7. Extrapolated values of the crossing temperatures $T_{\rm cross}(\infty, L_s)$ and $T^{\rm DM}_{\rm cross}(\infty, L_s)$ from the fits of Fig. 6, as a function of $1/L_s$, for different DM interaction $d$. SBC correspond to full symbols and FBC to open symbols. The case $d = 1$ with only SBC has also been added in this figure. The temperature axis has different scales for different values of $d$. The error bars are smaller than the symbol sizes.

but still quite comparable. However, $U_4^*$ for SBC and FBC are definitely different from each other. An average furnishes $U_4^* = 0.5851(7)$ for SBC and $U_4^* = 0.3536(69)$ for FBC. These results suggest that as soon as the DM interaction is present, the model changes its universality class. To check this point more carefully, the computation of critical exponents is valuable.

### C. Critical exponent $\nu$ and $\beta/\nu$ ratio

The critical exponent $\nu$ and the ratio $\beta/\nu$ can be obtained from the simulations by using the already-computed histograms and relations (9) and (10). The top left and bottom left panels in Fig. 10 show, respectively, the derivative $dU_4(\beta_T; L)/d\beta_T$ and the order parameter $m$ at $T_c$, both as a function of the lattice size $L$ (the axes are in base-10-logarithmic scale and this base has been kept in other log-log plots that are shown ahead in the text). From the scaling relations, one expects the slopes to furnish $\nu$ in the former case and $\beta/\nu$ in the latter case. However, although not completely apparent in Fig. 10, in some cases, residual finite-size effects are still present. To better estimate the critical exponents, several linear fits have been made by progressively discarding the smaller lattices. With $L_s$ now the smallest lattice size considered in the linear fit, we were able to get a good estimate of the critical exponents from $L_s = 8$ to $L_s = 32$. The corresponding results, as a function of $1/L_s$, are depicted in the right panels of Fig. 10, where it is easier to see that, in general, the finite-size effects are stronger for $d > 0$ and for FBC. These effects are more pronounced for $d = 0.5$ with FBC. The full lines in the right panels of Fig. 10 are additional linear fits to get the final estimate of the exponent.

As an example, for $d = 0$ (see the top right panel in Fig. 10), the extrapolated value of the correlation length critical exponent is $\nu = 0.713(2)$ with SBC and $\nu = 0.710(1)$

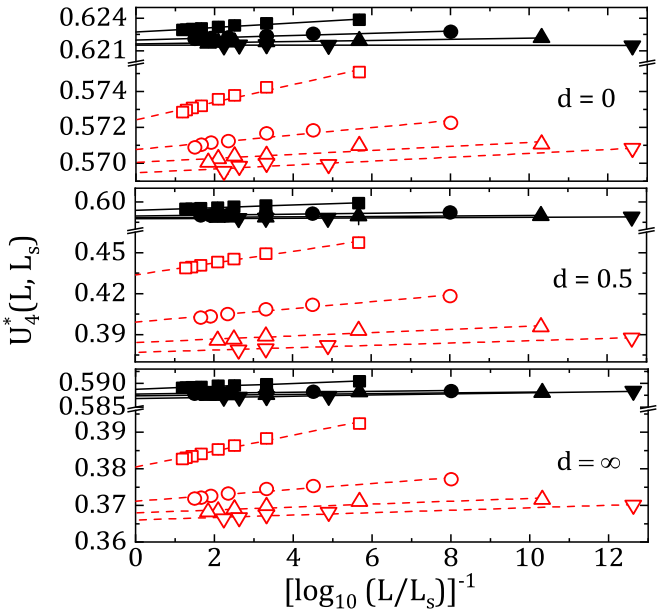


FIG. 8. Value of the cumulants $U_4^*(L, L_s)$, at the crossing temperatures $T_{\rm cross}(L, L_s)$ or $T^{\rm DM}_{\rm cross}(L, L_s)$, as a function of $[\log_{10}(L/L_s)]^{-1}$, computed from the simulations on the reference lattice of size $L_s$. The description of DM interaction, symbols, and lines given in Fig. 6 also applies to this figure [with the linear fits coming from Eq. (8) instead]. The error bars are smaller than the symbol sizes.

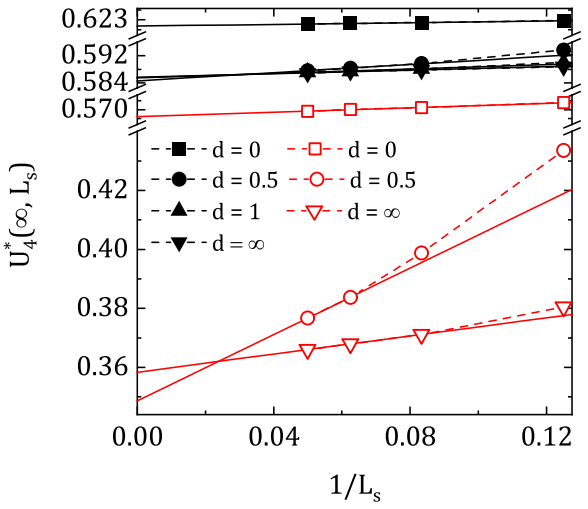


FIG. 9. Extrapolated values of the cumulants $U_4^*(\infty, L_s)$ from the fits of Fig. 8, as a function of $1/L_s$, for different DM interaction $d$ (here represented by different symbols) and SBC (full symbols) and FBC (open symbols). The case $d = 1$ with only SBC has also been added in this figure. The cumulant axis has different scales for different values of $d$ as well as for different boundary conditions. The full lines are linear fits, except for $d = 0.5$ FBC, which the straight line is defined by the two points that it passes through them. The dashed lines are just guides to the eye and the error bars are smaller than the symbol sizes.

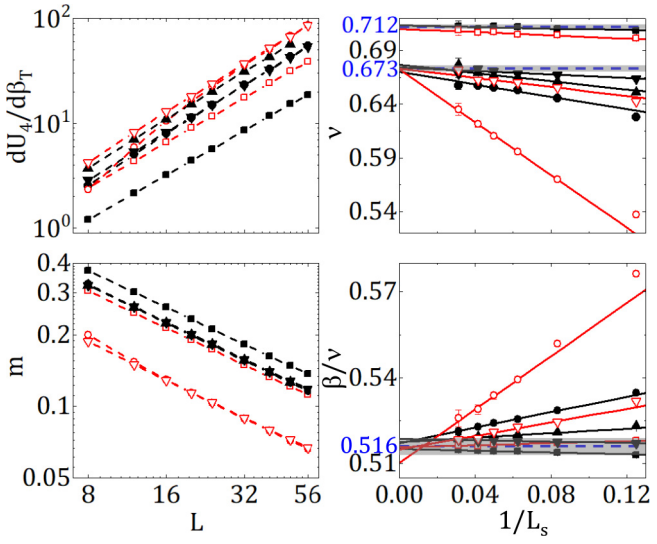


FIG. 10. Derivative of the order parameter fourth-order cumulant $dU_4(\beta_T; L)/d\beta_T$ (top left panel) and order parameter $m$ (bottom left panel), both as function of the lattice size $L$ and evaluated at $T = T_c$. In the left panels the axes scales are base-10-logarithmic and the dashed lines are just a guide to the eye. The linear fits, as described in the text, are shown for the critical exponent $\nu$ in the top right panel, and the ratio $\beta/\nu$ in the bottom right panel, as function of $1/L_s$ ($L_s$ here means the smallest considered lattice size), where full lines are additional linear fits. Horizontal dashed-lines in the two right panels indicate the mean values with the shaded area giving an idea of the error bars. The legends of Fig. 9 also apply in this case.

with FBC. As expected, $\nu$ should be independent of the boundary conditions. The present estimate gives $\nu = 0.712(2)$. It is interesting to see that for $d > 0$, all the extrapolations tend to the same result, independent of the values of $d$ and the type of boundary conditions. The corresponding average, represented by the horizontal dashed line in the top right panel in Fig. 10, gives $\nu = 0.673(3)$. This means, indeed, that the DM interaction does change the universality class of the model, as was suggested by the computation of the fourth-order cumulant in the previous subsection.

It is remarkable the extrapolations obtained for the ratio $\beta/\nu$ depicted in the bottom right panel of Fig. 10. Although for $d = 0.5$ and FBC we probably still need larger lattices with more MCS (which will take much more computational effort), for all the cases the extrapolations converge to the same region. This provides an estimate $\beta/\nu = 0.5155(4)$ for $d = 0$ and $\beta/\nu = 0.516(3)$ for $d \neq 0$, suggesting that besides having different exponents, the system satisfies the so-called weak universality class, where the exponents are different but their ratios are the same [45,46]. The final estimates of these critical exponents are listed in Table I.

In order to further seek whether the weak universality class really holds for this model, we have also computed the ratio $\gamma/\nu$ and $\alpha/\nu$ by using less CPU time.

### D. $\gamma/\nu$ and $\alpha/\nu$ ratios

The order parameter susceptibility $\chi$ and the specific heat $C$ have been obtained with less computational effort, as outlined by the second approach in Sec. III D, at the cost of having less precise data. Only one simulation comprising a total of $10^6$ MCS after relaxation, generating $10^5$ data points, was performed at temperature intervals $\Delta T = 0.001$ or $\Delta T = 0.0005$ close to the region of maximum values of the susceptibility and specific heat. In this way, for each lattice size $L$, not only $\chi_{\text{peak}}$ and $C_{\text{peak}}$ have been obtained but also the corresponding temperatures where these peaks occur. It was also possible to simulate the $L = 64$ lattice for $d = 0$, 0.5, and $d = \infty$ with SBC and FBC.

The FSS behavior of $\chi$ and $C$ are expressed by Eqs. (11) and (12). The peak temperature $T_{\text{peak}}$, where $T_{\text{peak}}$ can be either $T_{\chi_{\text{peak}}}$ or $T_{C_{\text{peak}}}$ has, for large-enough systems, a finite-size scaling relation given by [40,41]

$$T_{\text{peak}} \approx T_c + bL^{-1/\nu}, \tag{18}$$

where $b$ is a nonuniversal constant.

Figure 11 shows the peak temperature, $T_{\text{peak}}$, as a function of $L^{-1/\nu}$, obtained from the susceptibility and specific heat for different values of $d$ and boundary conditions. The $\nu$ exponents have been taken from the final universal ones in Table I. For $d = 0$, $\nu = 0.712$ and for all values $d \neq 0$, $\nu = 0.673$. In each data set, two linear fits have been made, one with all lattices and another one neglecting the smallest lattice $L = 8$. When the linear fits are quite different, which are apparent only for some cases in Fig. 11, the estimates come from fits neglecting the smallest lattice size. The corresponding results are displayed in Table I. It can be seen that the critical temperature from the susceptibility and specific heat are, for all values of $d$ and to within the error bars, in agreement

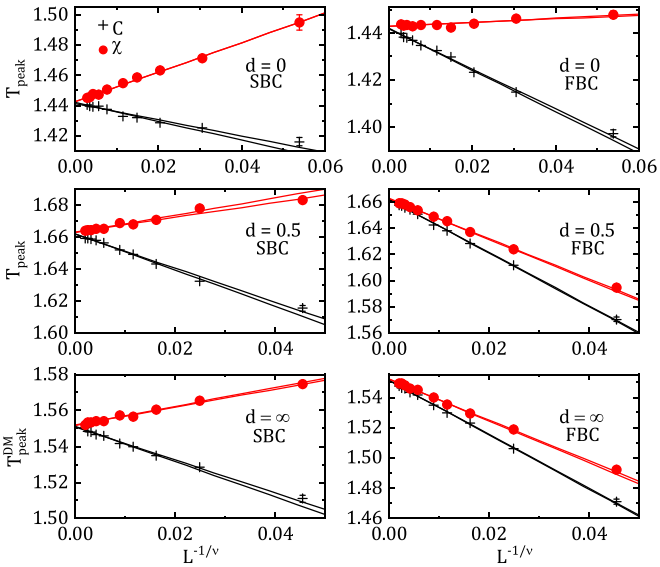


FIG. 11. Peak temperatures $T_{\text{peak}}$ and $T^{\text{DM}}_{\text{peak}}$ of the susceptibility (circles) and specific heat (crosses) as a function of $L^{-1/\nu}$ for different values of $d$ and respective boundary conditions. The exponents $\nu = 0.712(2)$ for $d = 0$ and $\nu = 0.673(3)$ for $d \neq 0$ are those obtained in this work and displayed in Table I. For each data set there are two lines coming from linear fits, one considering all lattices and another neglecting the smallest lattice size. The error bars are smaller than the symbol sizes.

with each other and also in agreement with the values of $T_c$ obtained from the cumulant crossings.

Figure 12 shows the logarithm of the order parameter susceptibility peak $\chi_{\text{peak}}$ as a function of the logarithm of the lattice size $L$ for different values of $d$. The slope of each data set furnishes, according to Eq. (11), the ratio $\gamma/\nu$. In this case,

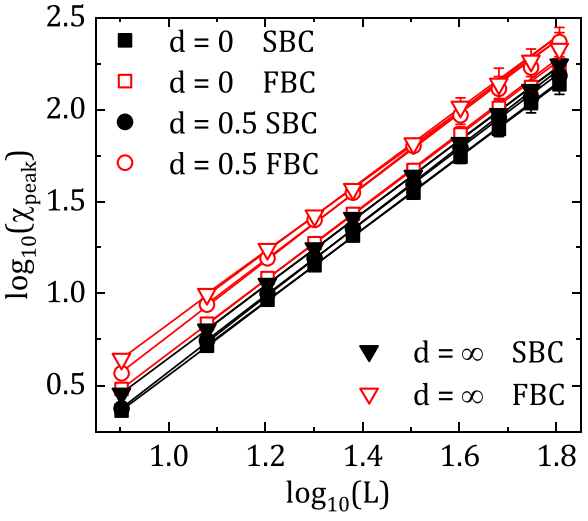


FIG. 12. Logarithm of the order parameter susceptibility peak $\chi_{\text{peak}}$ as a function of the logarithm of the lattice size $L$ for different values of $d$ with the boundary conditions specified in the legend. There are two lines corresponding to linear fits, one with all data and another neglecting the smallest lattice size. The error bars are smaller than the symbol sizes when they are not visible.

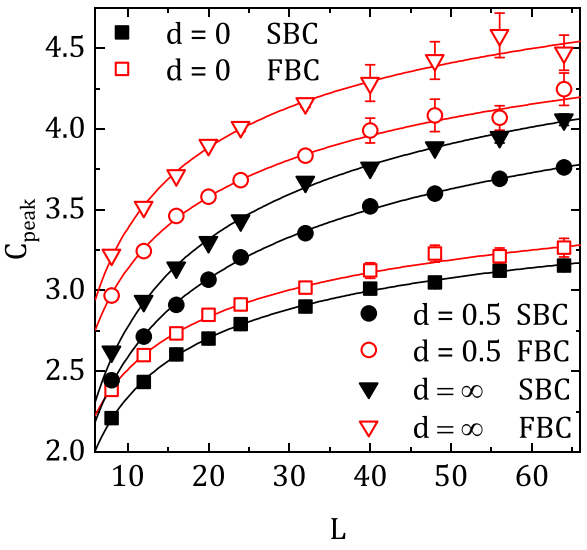


FIG. 13. Specific heat peak $C_{\text{peak}}$, as a function of the lattice size $L$, for different values of $d$ with the boundary conditions specified in the legend. Full lines are nonlinear fits according to Eq. (12) and considering all data for each value of $d$. The error bars are smaller than the symbol sizes when they are not visible.

due to the shorter MC runs, it is not possible to do the same analysis as for $\beta/\nu$. Nevertheless, for all values of $d$ the slopes from the fits neglecting the smaller lattice size $L = 8$ are close together, and the mean value is listed in Table I.

The specific heat peaks, as a function of $L$, for the same values of $d$ are shown in Fig. 13. It is clear that $\alpha$ is negative, since $C$ goes to a constant as $L \to \infty$. The full lines in Fig. 13 are fits using Eq. (12) and considering all data points. The corresponding values for $d$ different from zero have been averaged and are displayed in Table I. For comparison, the ratios $\alpha/\nu$ for $d = 0$ with SBC and FBC have also been averaged and given in this same table.

### E. Structure factor

The structure factor, $\mathcal{S}(\mathbf{q})$, has been measured for the same values of $d$ as before using single simulations as described in the previous subsection. Lattice sizes $L = 8,\ 12,\ 16,\ 20,$ and 24 have been used with SBC and FBC. The temperatures were $T_c$ for each value of $d$. The pair-correlation functions $\Gamma(\mathbf{r}_{jk})$ have been estimated at the final of the simulation, with their corresponding uncertainties. In this way, $\mathcal{S}(\mathbf{q})$ can be calculated, as a function of any arbitrary wave vector $\mathbf{q}$, through Eq. (15). Here $\mathbf{q}$ is measured in radians per lattice spacing, with the lattice spacing being defined as unity. The uncertainty in the structure factor has been estimated from the error propagation coming from $\Gamma(\mathbf{r}_{jk})$.

As an example, the static structure factor $\mathcal{S}(\mathbf{q})$ is shown in Fig. 14 for wave vectors in the $q_x$-$q_y$ plane for a lattice with size $L = 20$ at $T = T_c$ for various values of $d$. The same pattern is obtained when the wave vector lies either in the $q_x$-$q_z$ or $q_y$-$q_z$ planes. The intensity of the peaks, as well as their width, is indicated by the gradient scale on the right of each graph. Note that the peaks in $\mathcal{S}(\mathbf{q})$ occur at $q_x = q_y = \pm\phi$, where $\phi$ is the pitch angle. As one can see from the gradient intensities in

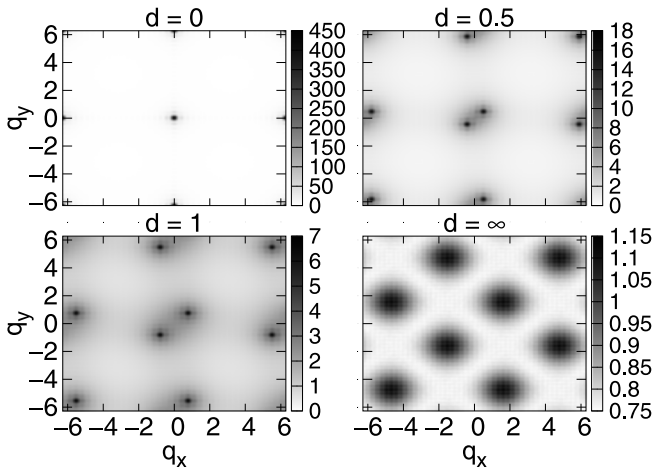


FIG. 14. Structure factor $\mathcal{S}(\mathbf{q})$ for the wave vector in the $q_x$-$q_y$ plane with $q_z = 0$ and $T = T_c$ for different values of $d$. The lattice size is $L = 20$ and SBC has been used in the MC simulations. The intensity of $\mathcal{S}(\mathbf{q})$ is given by the gradient scale on the right side of each figure.

Fig. 14, the height of the peaks gradually decrease, with their widths becoming wider, as $d$ increases from $d = 0$, ending up with the most spreading values, close to unity, for $d = \infty$.

In order to extract more quantitative results from these calculations, we have checked if there is any finite-size scaling of the maximum value of $\mathcal{S}(\phi, \phi, 0)$ on the system size $L$. The graph on the top panel in Fig. 15 shows, for the same $d$ values considered in Fig. 14, a plot of the peak of $\mathcal{S}(\phi, \phi, 0)$, as a function of $L = 8$, 12, 16, 20, and 24, where both axes are logarithmic. In this case, we have also included some results from simulations with FBC performed at $T = T_c$. As it is expected, the model without DM interaction ($d = 0$ and $\phi = 0$) exhibits the usual long-range magnetic ordering along the planes in the lattice, as it can be clearly seen in the behavior of $\mathcal{S}(0, 0, 0)$ that increases as $L$ increases and tends to infinity in the thermodynamic limit. However, for $d \neq 0$, the peaks $\mathcal{S}(\phi, \phi, 0)$ do not show any regular increase as $L$ increases. Instead, the points tend to saturate or fluctuate around a horizontal line. This means that looking at $x$-$y$, $x$-$z$, and $y$-$z$ planes in the lattice, one does not observe any long-range magnetic ordering.

On the other hand, it is interesting to analyze $\mathcal{S}(\mathbf{q})$ when $\mathbf{q} = \pm(\phi, \phi, \phi)$, a wave vector being parallel to the diagonal direction of the lattice or, in terms of crystallographic definitions, the [111] direction in a simple cubic lattice. The corresponding peaks of $\mathcal{S}(\mathbf{q})$ at $T = T_c$, as a function of $L$, in logarithmic scales, are shown in the bottom panel of Fig. 15. The two curves for $d = 0$ have not changed their behavior in relation to those in the upper panel. However, for all of the remaining curves with $d \neq 0$, $\mathcal{S}(\phi, \phi, \phi)$ follow now the same trend as for $d = 0$, namely increasing with $L$ and diverging to infinity in the thermodynamic limit. In other words, the magnetic long-range ordering for $d \neq 0$ is observed when the wave vector $\mathbf{q}$ is oriented along the diagonal directions with specific values that depend on $d$ through the pitch angle $\phi$. This result agrees with a theoretical finding for this model [21], which shows that the magnetization changes in a spiral

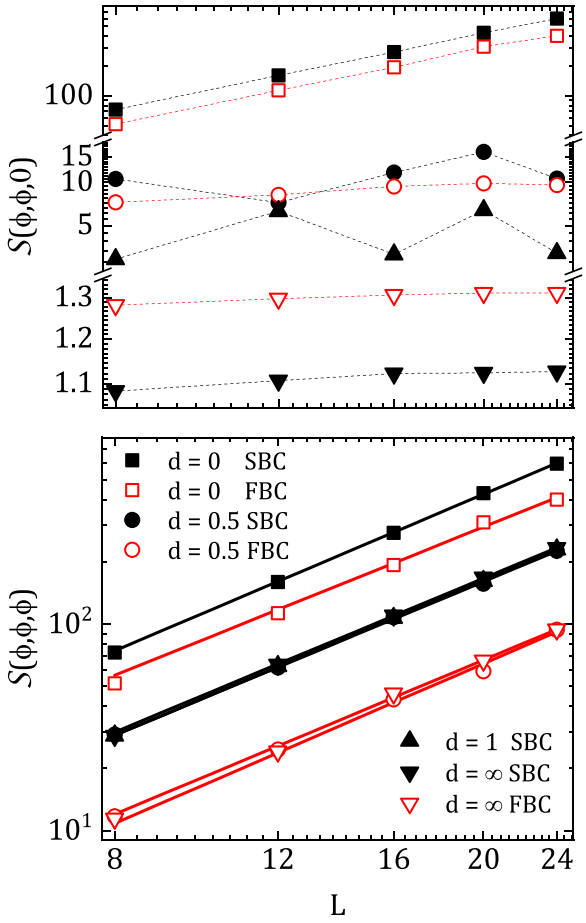


FIG. 15. Peak values of the static structure factor $\mathcal{S}(\mathbf{q})$, for wave vectors $\mathbf{q} = \pm(\phi, \phi, 0)$ (upper panel) and $\mathbf{q} = \pm(\phi, \phi, \phi)$ (bottom panel), as a function of the lattice size $L$. The results are at $T = T_c$ for each $d$ indicated in the legends (valid also for the top panel). Both axes are base-10-logarithmic. Dashed lines are only guides for the eye while solid lines are linear fits to the data. The error bars are smaller than the symbol sizes.

way with rotations around the $z$ axis with a wave vector $\mathbf{q} = \pm(\phi, \phi, \phi)$.

It is also remarkable that all curves in the bottom graph of Fig. 15 follow a power law and are almost parallel to each other. In fact, by the static structure factor definition in Eq. (15), one can verify that $\mathcal{S}(\phi, \phi, \phi) \approx \mathcal{S}_0 L^{\gamma/\nu}$ when $T = T_c$. Although the lattice sizes in this case are not as large as those used in the susceptibility and specific heat peaks analysis, we have additionally performed linear fits to all data in the bottom panel of Fig. 15. The estimate from the average is $\gamma/\nu = 1.9(1)$, in good agreement with the previous values from the order parameter susceptibility of the last section (despite the larger error due to the less statistics in this case).

The oscillations present in $\mathcal{S}(\phi, \phi, 0)$ as a function of $L$, depicted in the top panel of Fig. 15, deserve more attention. So in order to obtain extra insight about the $\mathcal{S}(\mathbf{q})$ behavior as a function of $\mathbf{q}$, $\phi$ and $L$, we defined the quantity $\widetilde{\mathcal{M}}(\mathbf{q}) = \| \sum_{j=1}^{L^3} \mathbf{S}_j e^{-i\mathbf{q}\cdot\mathbf{r}_j} \| / L^3$, analogously to an order parameter, although assuming complex values (the two double-vertical bars on the right hand side in the above equation represent

the vector modulus). Then, the structure factor is given by $\mathcal{S}(\mathbf{q}) = L^3|\widetilde{\mathcal{M}}(\mathbf{q})|^2$, where the vertical bars refer to the modulus of the complex $\widetilde{\mathcal{M}}(\mathbf{q})$.

Considering the ground-state spin configuration, the structure factor for a lattice size $L$ can be written in analytical form,

$$\mathcal{S}(\mathbf{q}) = \frac{1}{2L^3}\prod_{j=1}^{3}\left(\left\{\frac{\sin[(\phi+q_j)L/2]}{\sin[(\phi+q_j)/2]}\right\}^2 + \left\{\frac{\sin[(\phi-q_j)L/2]}{\sin[(\phi-q_j)/2]}\right\}^2\right), \tag{19}$$

where the index $j = 1, 2, 3$ labels the $x$, $y$, and $z$ wavevector components, respectively. In the case $\mathbf{q} = \pm(\phi, \phi, 0)$, Eq. (19) simplifies into

$$\mathcal{S}(\phi,\phi,0) = \frac{1}{2L^3}\left\{\left[\frac{\sin(L\phi)}{\sin\phi}\right]^4 + L^4\right\}\left[\frac{\sin(L\phi/2)}{\sin(\phi/2)}\right]^2. \tag{20}$$

Figure 16 is a plot of the above structure factor for $d = 0.5$, 1, and $\infty$ as a function of $L$, both quantities on logarithmic scale. It is patent the similarity of the data at $T = 0$ with those obtained at $T = T_c$ depicted in the top panel of Fig. 15. Nevertheless, here it becomes easier to understand the oscillations as $L$ changes, because the structure factor is zero whenever $\sin(L\phi/2) = 0$. One can still infer that one has a FSS behavior for lattices that are commensurate with the pitch angle and a different FSS for incommensurate lattices. This is clearly seen for $d = 1$ and $d = \infty$, the latter one being valid for all data because all lattice sizes are commensurate with the pitch angle. However, for $d = 0.5$, none of the $L$ values turn out to be commensurate and the data do not follow any special scaling.

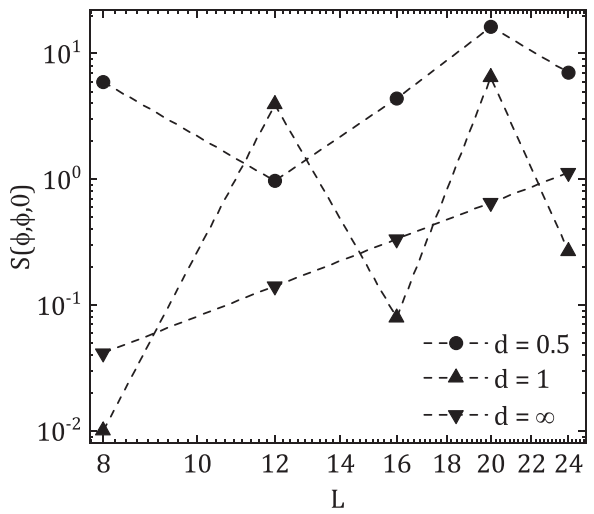


FIG. 16. Peak values of the static structure factor $\mathcal{S}(\mathbf{q})$, for wave vector $\mathbf{q} = \pm(\phi, \phi, 0)$ as a function of lattice size $L$ according to Eq. (20). The results are at $T = 0$ for each $d$ shown in the legend. Both axes are base-10-logarithmic. Dashed lines are only guides to the eyes.

Finally, for the wave vector $\mathbf{q} = \pm(\phi, \phi, \phi)$, Eq. (19) results in

$$\mathcal{S}(\phi,\phi,\phi) = \frac{1}{2L^3}\left\{\left[\frac{\sin(L\phi)}{\sin\phi}\right]^6 + L^6\right\}, \tag{21}$$

which does not have any zeros for $L > 0$ and increases as $L^3$.

### F. Phase diagram

Still shorter simulations were done just to locate the transition temperature for further values of $d$. These transitions have been estimated using cumulant crossings between lattices $L = 32$ and $L = 24$ only, with SBC (FBC gives similar estimates). Although such estimates are, in fact, underestimated in comparison to that for the infinite system, the error in the values of $T_c$ are relatively small when viewed in the whole temperature range under consideration. With this additional data it is possible to have a good picture of the global phase diagram in the $T$-$d$ plane as depicted in Fig. 17.

The main figure shows the reduced temperature $T_c(d)/T_c^{\mathrm{DM}}$ as a function of $d$. With this definition, the asymptotic behavior of $T_c(d)/T_c^{\mathrm{DM}}$, in the $d = \infty$ limit (given by the dashed

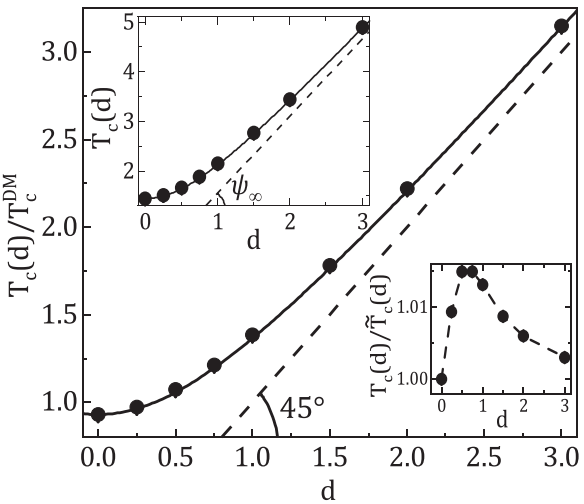


FIG. 17. Phase diagram in the temperature versus DM interaction plane. The circles are the present results and the full lines are fits to a hyperbolic function as described in the text. The dashed lines are the slopes of the transition lines in the limit $d = \infty$. The main graph shows the normalized transition temperature $T_c(d)/T_c^{\mathrm{DM}}$, where the asymptote slope is 45°. The top inset gives $T_c(d)$, where the asymptote slope is $\psi_\infty$. The bottom inset shows the ratio $T_c(d)/\widetilde{T}_c(d)$. The error bars are smaller than the symbol sizes.

line), has a declivity of 45°. The top inset shows $T_c(d)$ as a function of $d$ for comparison. In this case, the asymptotic behavior of the transition line is such that $\tan\psi_\infty = T_c^{\rm DM}$.

It is well known that the XY model with DM interaction has an exact hyperbolic expression for the critical temperature, as a function of DM interaction, that depends only on the critical temperature for $d = 0$ [32,35]. To test whether such behavior also applies to the Heisenberg model, we have performed a fit of the ratio $T_c(d)/T_c^{\rm DM}$ to a branch of a hyperbola defined as

$$\widetilde{T}_c(d) = T_c^{\rm DM}\sqrt{r^2 + d^2}, \tag{22}$$

$$r = \frac{T_c(0)}{T_c^{\rm DM}}, \tag{23}$$

where $T_c(0)$ is the critical temperature of the Heisenberg model and $r$ is the only adjustable parameter. The full line in the upper inset in Fig. 17 is given by setting $T_c(0) = 1.44293(5)$ and $T_c^{\rm DM} = 1.55183(1)$ (see Table I), resulting in $r = 0.92982(3)$. The fit in the main graph, shown as a full line, gives $r = 0.92982(7)$. Naturally, the data do not follow a hyperbolic function, as can be seen in the bottom inset. It shows that the ratio $T_c(d)/\widetilde{T}_c(d)$ has a systematic deviation, with the largest deviation around $d \approx 0.625$ and asymptotically decreasing to unity as $d$ tends to infinity. However, the fitted line can give good estimates of the critical temperature for any different values of the DM interaction $d$.

## V. CONCLUDING REMARKS

The main results of the present Monte Carlo study of the Heisenberg model with DM interaction are conveyed in Table I. The first comparison is for the model with $d$=0, where there are ample results in the literature for the isotropic Heisenberg model from different techniques, including experimental measurements of the critical exponents. The transition temperature, in this case $T_c = 1.44295(3)$, is in excellent agreement with previous MC simulations, e.g., $T_c = 1.442987(1)$ [48] and $T_c = 1.44293(6)$ [51].

Unlike the critical temperature and critical exponents, the fourth-order cumulant of the order parameter depends on the boundary conditions. From an analysis of the universal quantities given in Table I, it is also apparent that the critical exponents along the transition line for $d > 0$ are different from the isotropic Heisenberg model. However, as the ratio of the critical exponents and the cumulants are the same, to within the error bars, it is evident that *weak universality* holds for the Heisenberg model with DM interaction. Moreover, from a comparison of the exponents for $d > 0$ and those in the literature for the XY model, it is evident that the Heisenberg model with DM interaction is in the same weak universality class as the XY model [19–21].

Additional numerical comparison to other MC simulations as well as different approximation methods can be found in Refs. [52,53].

## ACKNOWLEDGMENTS

This work has been partially funded by CNPq, CAPES, and FAPEMIG (Brazilian agencies) and computationally supported, in part, by resources and technical expertise from the Georgia Advanced Computing Resource Center (GACRC), a partnership between the University of Georgia's Office of the Vice President for Research and Office of the Vice President for Information Technology. We also acknowledge Prof. Gerald Weber for the invaluable assistance in the use of the Statistical Mechanics Computer Lab facilities at UFMG.

[1] W. Heisenberg, Z. Phys. **49**, 619 (1928).
[2] R. A. Erickson, Phys. Rev. **90**, 779 (1953).
[3] A. S. Borovik-Romanov and M. P. Orlova, Sov. Phys. JETP **4**, 531 (1957).
[4] T. Matsubara and H. Matsuda, Prog. Theor. Phys. **16**, 569 (1956).
[5] T. Moriya, Phys. Rev. Lett. **4**, 228 (1960).
[6] A. Crépieux and C. Lacroix, J. Magn. Magn. Mater. **182**, 341 (1998).
[7] M. Uchida, Y. Onose, and Y. Matsui, Science **311**, 359 (2006).
[8] Y. Kousaka, S.-I. Yano, J.-I. Kishine, Y. Yoshida, K. Inque, K. Kikushi, and J. Akimitsu, J. Phys. Soc. Jpn. **76**, 123709 (2007).
[9] S. M. Stishov and A. E. Petrova, Phys. Usp. **54**, 1117 (2011).
[10] J. Kishine and A. S. Ovchinnikov, *Theory of Monoaxial Chiral Helimagnet*, edited by R. E. Camley and R. L. Stamps, Solid State Physics Vol. 66 (Academic Press, San Diego, CA, 2015), pp. 1–130.
[11] M. Bode, M. Heide, K. V. Bergmann *et al.*, Nature (Lond.) **447**, 190 (2007).
[12] P. Ferriani, K. von Bergmann, E. Y. Vedmedenko, S. Heinze, M. Bode, M. Heide, G. Bihlmayer, S. Blugel, and R. Wiesendanger, Phys. Rev. Lett. **101**, 027201 (2008).
[13] S. V. Grigoriev, Y. O. Chetverikov, D. Lott, and A. Schreyer, Phys. Rev. Lett. **100**, 197203 (2008).
[14] W. Jiang, G. Chen, K. Liu, J. Zang, S. G. E. te Velthuis, and A. Hoffmann, Phys. Rep. **704**, 1 (2017).
[15] B. Göbel, I. Mertig, and O. A. Tretiakov, Phys. Rep. **895**, 1 (2021).
[16] H. Yang, J. Liang, and Q. Cui, Nat. Rev. Phys. **5**, 43 (2023).
[17] Y. Tokunaga, T. Kimura, and T.-H. Arima, J. Phys. Soc. Jpn. **92**, 081008 (2023).
[18] T. Tolinski and K. Synoradzki, Intermetallics **47**, 1 (2014).
[19] J. H. H. Perk and H. W. Capel, Phys. Lett. A **58**, 115 (1976).
[20] M. Calvo, J. Phys. C: Solid State Phys. **14**, L733 (1981).
[21] L. Klein and A. Aharony, Phys. Rev. B **44**, 856 (1991).
[22] K. Y. Ho, T. R. Kirkpatrick, Y. Sang, and D. Belitz, Phys. Rev. B **82**, 134427 (2010).
[23] V. Laliena, J. Campo, and Y. Kousaka, Phys. Rev. B **94**, 094439 (2016).
[24] F. Azizi and H. Rezania, Physica E **114**, 113603 (2019).
[25] S. D. Yi, S. Onoda, N. Nagaosa, and J. H. Han, Phys. Rev. B **80**, 054416 (2009).
[26] A. Hamann, D. Lamago, T. Wolf, H. v. Löhneysen, and D. Reznik, Phys. Rev. Lett. **107**, 037207 (2011).
[27] S. Buhrandt and L. Fritz, Phys. Rev. B **88**, 195137 (2013).
[28] M. Shinozaki, S. Hoshino, Y. Masaki, J. Kishine, and Y. Kato, J. Phys. Soc. Jpn. **85**, 074710 (2016).

[29] Y. Nishikawa and K. Hukushima, Phys. Rev. B **94**, 064428 (2016).
[30] A. M. Belemuk and S. M. Stishov, Phys. Rev. B **95**, 224433 (2017).
[31] H. Liu, J. A. Plascak, and D. P. Landau, Phys. Rev. E **97**, 052118 (2018).
[32] G. A. Silva, J. A. Plascak, and D. P. Landau, Phys. Rev. E **106**, 044116 (2022).
[33] M. Elhajal, B. Canals, R. Sunyer, and C. Lacroix, Phys. Rev. B **71**, 094420 (2005).
[34] E. Y. Vedmedenko, L. Udvardi, P. Weinberger, and R. Wiesendanger, Phys. Rev. B **75**, 104431 (2007).
[35] F. C. Alcaraz and W. F. Wreszinski, J. Stat. Phys. **58**, 45 (1990).
[36] N. Metropolis, A. W. Rosenbluth, M. N. Rosenbluth *et al.*, J. Chem. Phys. **21**, 1087 (1953).
[37] W. H. Press, S. A. Teukolsky, W. T. Vetterling, and B. P. Flannery, *Numerical Recipes in C: The Art of Scientific Computing*, 2nd ed. (Cambridge University Press, Cambridge, UK, 1988 and 1992).
[38] P. Olsson, Phys. Rev. Lett. **73**, 3339 (1994).
[39] K. Binder, Z. Phys. B: Condens. Matter **43**, 119 (1981).
[40] C. Holm and W. Janke, Phys. Rev. B **48**, 936 (1993).
[41] D. P. Landau and K. Binder, *A Guide to Monte Carlo Simulation in Statistical Physics*, 5th ed. (Cambridge University Press, Cambridge, UK, 2021).
[42] W. Zhu, S.-S. Gong, and D. N. Sheng, Proc. Natl. Acad. Sci. USA **116**, 5437 (2019).
[43] R. Yadav, S. Nishimoto, M. Richter, J. van den Brink, and R. Ray, Phys. Rev. B **100**, 144422 (2019).
[44] W. Selke, Eur. Phys. J. B **51**, 223 (2006).
[45] M. Suzuki, Prog. Theor. Phys. **51**, 1992 (1974).
[46] N. Khan, P. Sarkar, A. Midya, P. Mandal, and P. K. Mohanty, Sci. Rep. **7**, 45004 (2017).
[47] M. Campostrini, M. Hasenbusch, A. Pelissetto, and P. Rossi, and E. Vicari, Phys. Rev. B **63**, 214503 (2001).
[48] Y. Nonomura and Y. Tomita, Phys. Rev. E **93**, 012101 (2016).
[49] M. Krech and D. P. Landau, Phys. Rev. B **60**, 3375 (1999).
[50] M. Campostrini, M. Hasenbusch, A. Pelissetto, and E. Vicari, Phys. Rev. B **74**, 144506 (2006).
[51] K. Chen, A. M. Ferrenberg, and D. P. Landau, Phys. Rev. B **48**, 3249 (1993).
[52] A. Pelissetto and E. Vicari, Phys. Rep. **368**, 549 (2002).
[53] W. Xu, Y. Sun, J.-P. Lv, and Y. Deng, Phys. Rev. B **100**, 064525 (2019).